Materials Characterization 159 (2020) 110002

Contents lists available at ScienceDirect

Materials Characterization

journal homepage: www.elsevier.com/locate/matchar

# Microstructure and tensile response of friction stir welded Al–Cu–Li (AA2198-T8) alloy

Niraj Nayan[a,b], Manasij Yadava[c], Rajdeep Sarkar[d], S.V.S. Narayana Murty[a,*], N.P. Gurao[c], Sivasambu Mahesh[e], M.J.N.V. Prasad[b], I. Samajdar[b]

[a] Vikram Sarabhai Space Centre, Indian Space Research Organization, Trivandrum, 695022, India
[b] Department of Metallurgical Engineering and Materials Science, Indian Institute of Technology Bombay, Mumbai, 400076, India
[c] Department of Materials Science and Engineering, Indian Institute of Technology Kanpur, Kanpur, 208016, India
[d] Defence Metallurgical Research Laboratory, Hyderabad, 500 058, India
[e] Department of Aerospace Engineering, Indian Institute of Technology Madras, Chennai, 600 036, India

ARTICLE INFO

*Keywords:*
Al-Cu-Li alloy
Friction stir welding
Precipitation
Digital image correlation
Strain hardening

ABSTRACT

Friction stir welds (FSWs) can be considered as an ensemble of elements of material with composite microstructures connected in series. In the present study, bead-on-plate FSW runs were made on an Al–Cu–Li alloy with varying rotation speeds ranging from 400 to 800 rpm. Microstructure of the FSW region was investigated by using optical microscope, electron backscattered diffraction (EBSD) and transmission electron microscope (TEM). Thermal stability of various precipitates was evaluated with differential scanning calorimetry (DSC) measurements. Strength variation across FSW cross sections was mapped by microhardness measurements. Average as well as local mechanical properties were evaluated using a digital image correlation (DIC) technique. Irrespective of the process parameters, FSW samples showed similar tensile and strain hardening behaviour along with serrations in stress-strain curves while local strength values showed increasing trend with rotation speed. The FSW alloy produced at intermediate rotation speed exhibited different mechanical behavior and is correlated with the resultant substantial changes in the microstructure. Strain localization occurred at the boundary of nugget zone and thermo-mechanically affected zone which led to failure of the FSW tensile specimens within weld regions. Fractography investigation revealed that the failure is initiation controlled, that is void nucleation at coarse precipitate-matrix interfaces.

## 1. Introduction

Fusion welding of Al–Li alloys has posed serious problems like evaporation loss of Li, weld cracking, distortion due to high residual stresses and weld porosity due to high solubility for hydrogen [1]. All of these led to deleterious effect on mechanical properties [2–4] and thereby the structural integrity. These limitations and shortcoming of fusion welding have been eliminated by the invention of friction stir welding (FSW). FSW is a solid state joining process invented by Thomas et al. [5] at The Welding Institute (TWI) in the UK. FSWed (read as friction stir welded) joint formation occurs by mechanical mixing of the plasticized material on the two sides of the faying surfaces. The heat evolution during FSW required for softening of base material around tool is due to frictional and adiabatic heating [6,7]. It is controlled by welding parameters, geometry and dimensions of tool shoulder, tool pin, workpiece thickness, and thermal conductivities of workpiece and anvil [7].

The heat generated during FSW affects the microstructure of the base material structure in age hardenable aluminum alloys and various steels [8–11]. This leads to a variation in microstructure within and around the processed region [12–19]. The central region near seam, known as stir zone (SZ) or nugget zone (NZ), experiences peak temperatures and dynamically recrystalizes during FSW. The surrounding material which has been thermo-mechanically processed but did not undergo complete recrystallization is known as thermo-mechanically affected zone (TMAZ). The outer most region of the processed zone which has only been affected thermally and has not been deformed during FSW is known as heat affected zone (HAZ) [7]. This variation in microstructure is enhanced while welding age hardenable e.g. 2XXX, 6XXX or7XXX series aluminium alloys [4,20–24]. The heterogeneity in microstructure can affect the mechanical properties across FSW which significantly reduces the load carrying ability of the welded material.

* Corresponding author. Material Characterisation Division, Materials and Metallurgy Group, Vikram Sarabhai Space Centre, Trivandrum, 695 022, India.
*E-mail address:* susarla.murty@gmail.com (S.V.S.N. Murty).

https://doi.org/10.1016/j.matchar.2019.110002
Received 1 August 2019; Received in revised form 7 October 2019; Accepted 5 November 2019
Available online 11 November 2019

Al–Cu–Li based age hardenable alloy, AA2198 [25–28] has attracted major attention in recent years in aerospace industries as a replacement of AA2024/AA7475 alloys for fuselage skin applications in commercial aircrafts due to its low density, outstanding combination of static strength and damage tolerance [29,30]. The strengthening in AA2198 in T8 temper is achieved by precipitation of thin platelets of $T_1$, θ′ and also GP zones [26–28]. The δ′ precipitate in AA2198-T8 has been reported to be absent due to less than 1% Li concentration [31,32]. FSW of AA2198 alloys was studied by various researchers to investigate different aspects of the process [33–41]. A 91% strength of the base metal (BM) in T3 temper (base yield strength, YS of 275 MPa) [15] and 60–80% in T8 temper (base YS of ~430 MPa) [17,42,43] was reported in literature. FSW process parameters like rotation and traverse speeds have not been found to have any noticeable effect on the weld strength in both tempers [17,19] but an effect on the strength variation was noticed through microhardness profiles. Both 'U' shape [38] and 'W' shape [44] profiles were reported in literature with 85–90 HV minima in Vickers hardness. The profile shapes were attributed to the local peak temperatures and thermal cycles during FSW [14,45,46]. In U shape hardness profile the SZ consists of either full solid solution [42,47] or with solution and some coarse precipitates of θ′, $T_B$ particles [34,44]. In W shape profiles the nugget centre hardness recovers by formation of clusters during natural aging after FSW. TEM investigations by Malard et al. [48] have shown that TMAZ and HAZ microstructures consist of partially dissolved and coarsened $T_1$ precipitates. Wang et al. [17] in their work with Bobbin tool FSW of AA2198-T851, reported widening of the minima away from weld seam and shrinking of each valley in the W shape profile with increase in rotation speed.

Heterogeneous strength distribution, as evidenced by microhardness profiles, results in non-uniform strain distribution in the FSW samples when loaded in transverse direction. DIC has been used to measure the strain distribution and strain localization in FSW specimens during tensile test [42,49,50]. For example, Jolu et al. [38] have shown that strain localization occurred in the TMAZ area on both sides of the weld. DIC technique can also be used to evaluate local tensile behaviour. Lockwood and co-workers [51,52] and Genevois et al. [53] have established that local stress conditions in FSW are iso-stress in nature and mechanical behaviour obtained from surface measurements agree well with bulk mechanical behaviour. Reynolds and Duvall [54] proposed a DIC based technique to determine the constitutive behaviour of FSW welds. This technique was utilized by Leitao et al. [50] to determine local ultimate tensile strength of different regions across FSW.

As mentioned above there has been substantial research work on the microstructure and mechanical properties of FSWed AA2198 alloy but most of the reported works were based on FSW made with one set of process parameters. Moreover, very little attention has been given to the strain hardening aspects of the welded joint as a whole and less so on the local strain hardening behaviour in different zones of the weld. This study is essential for structural aerospace designers for effective utilisation of the full potential of the FSWed Al–Cu–Li alloys. Therefore, the microstructure evolution, tensile strength and strain hardening behaviour of bead on plate (BoP) FSW of AA2198-T84 sheets was undertaken in the present study. Local mechanical behaviour of various zones was obtained from the DIC analysis utilizing the methodology presented by Reynolds and Duvall [54] and is correlated with microstructure. Mechanical behaviour of the joints was correlated with the local microstructure details determined through TEM and DSC measurements.

## 2. Material and experimental methods

### 2.1. Material

The present study was conducted on a 2.2 mm thick sheet of AA2198 alloy in the T8 temper (solution treatment, water quenching, cold work and peak aged). The alloy contained (by wt.) 3.2%Cu, 1.0% Li, 0.3%Mg, 0.1%Zr and 0.4%Ag as the main alloying elements.

### 2.2. FSW

Bead on plate FSW was conducted on 120 mm × 200 mm coupons for about 190 mm run length. Tool was made of H13 tool steel in hardened condition and had a shoulder diameter of 12 mm, with the conical frustum shaped pin having top diameter of 6 mm, a bottom diameter of 4 mm and 2.0 mm pin height. Runs were made with a tilt of 2°. To study the effect of rotation speed, FSW runs were made on coupons with 400, 600 and 800 rpm (clockwise) and a traverse speed of 200 mm/min. FSW was carried out perpendicular to the rolling direction.

### 2.3. Metallography, characterization and mechanical testing

Cross sections of the FSW runs were polished on a series of abrasive papers followed by disc polishing using alumina and one-micron diamond paste for metallographic examinations. The polished surfaces were etched with Keller's reagent (95 mL water, 2.5 mL $HNO_3$, 1.5 mL HCl, 1.0 mL HF) and observed under OLYMPUS BX51 M microscope. Microhardness measurements were made on the cross sections covering a 30 mm × 2 mm area with the FSW region at the middle. Measurements were taken under 100 g load, 10s dwell time and at an interval of 1 mm along horizontal direction and 0.5 mm in the vertical direction. Thus, nearly 120 indents were taken on each sample and then microhardness maps were constructed from the collected data.

Samples for the differential scanning calorimetry (DSC) and transmission electron microscopy (TEM) were collected from two different locations, namely nugget zone (NZ) region and NZ-TMAZ region towards advancing side of the FSW samples. DSC (Netzsch) was conducted at a heating rate of 10 °C $min^{-1}$ from room temperature to 500 °C under a continuous circulation of high purity argon gas. The DSC was calibrated as per the standard practice suggested in Refs. [55,56]. Thin foils for TEM were prepared using 3 mm discs spark cut from mechanically ground strips of 0.15 mm thickness. These ground discs were then electropolished with twin jet electro polisher with $HNO_3$-methanol solution in 1:3 ratio at −20 °C. TEM was carried out on a FEI TECHNAI20 TEM operating at 200 kV. Cross section samples metallographically polished up to 1 μm surface finish were further electropolished using Struers A2 electrolyte. Electron backscattered diffraction (EBSD) was performed in FEI™ Quanta 3D-FEG (field emission gun) scanning electron microscope (SEM) with a step size of 0.2 μm.

Flat tensile specimens, as per ASTM-E8 standards with a gauge length of 32 mm and gauge width of 2 mm, were cut across the welds. Samples were polished to remove the surface markings and sheet thinning caused by shoulder digging into the sheets. One specimen was also tested without surface polish to evaluate the effect of shoulder digging on the tensile strength. Parent material in T8 temper was tested for comparison purpose along with one specimen in T4 temper (Solution treatment + natural aged). Tensile testing was performed in a screw driven Instron 3369 universal testing machine with 1.9 mm/min crosshead speed equivalent to an initial strain rate of $1 \times 10^{-3}$ $s^{-1}$.Three specimens were tested for each FSW condition. The failed specimens were taken for fractography analysis in SEM.

One of the polished tensile specimens from each run was etched to mark the edges of the processed zone before making the speckle pattern for digital image correlation (DIC). This helped in identification of the NZ and TMAZ locations. For DIC setup, speckle pattern on the gauge length of the specimens were made and the patterns were recorded at 30 frames per second speed. An open source DIC code available at Mathworks® (developed by Chris Eberl, Robert Thompson, Daniel Gianola and Sven Bundschuh) was used to process the data. The displacement and strain fields obtained from the DIC analysis were averaged over two different locations of NZ and TMAZ of FSW to obtain

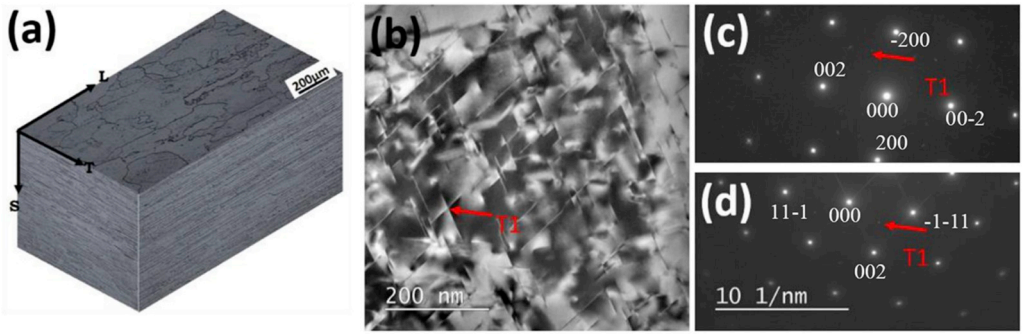


**Fig. 1.** (a) Triplanar optical micrographs of the as-received AA2198 alloy, (b) bright-field TEM micrograph of the parent material, and SADP in (c) < 100 > and (d) < 110 > zone axes.

average strain for each image frame. These strain values were then used to calculate instantaneous cross sectional area which were further used to calculate local true stress from the measured load for the corresponding image frame. Work by Reynolds et al. [51] and Leitao et al. [47] can be referred for details of the procedure to calculate local stress values from DIC data.

## 3. Results

Triplanar optical microstructures of the parent material (in T8 temper) are shown in Fig. 1a. It shows large grains of 200–400 μm in rolling (L) direction and pancaked elongated grains, typical of sheet microstructure, in transverse (T) and short transverse(S) direction. Bright-field TEM image along $< 110 >_{Al}$ projection in Fig. 1b and corresponding selected area electron diffraction patterns (SADP) in Fig. 1(c and d) indicate presence of the main strengthening phase $T_1$ ($Al_2CuLi$) in the matrix.

Forces and torques on the spindle during FSW are plotted in Fig. 2. Z-force lie within 600 N–900 N range and torque values decreased from ~21 Nm for 400 rpm to ~13 Nm for 800 rpm. Macrographs (montage of series of optical images) shown in Fig. 2 for cross-sections of FSW regions of three different rotation speeds clearly indicate that all the FSW runs were defect-free through sheet thickness (Fig. 3). Processed zones exhibited a “basin” shape, a typical characteristic of FSW. The symmetry of the nugget zone increased with increase in the rotation speed.

### 3.1. Microstructure of FSWed AA2198 alloy

Fig. 4 shows the colored inverse pole figure (IPF) maps obtained by EBSD of nugget zone regions of three FSW samples with different rotation speeds. The average grain size of the FSW nugget zones for the 400, 600 and 800 rpm are ~6, ~2 and ~12 μm respectively. The sample processed at 600 rpm has smallest grain size and narrow grain size distribution in the nugget zone as compared to the sample processed at 400 rpm and 800 rpm.

TEM micrographs of NZ of FSW samples are shown in Fig. 5. All images show the presence of fine equiaxed grains with well-defined grain boundaries due to the occurrence of dynamic recrystallization (Fig. 5c,f,g, j). Very few scattered dislocations, some in the form of dislocation spirals were noticed. GP zones were observed in all three samples (Fig. 5b,e,h). Intensity of these streaks was higher in 600 and 800 rpm samples as compared to in 400 rpm sample. Apart from $Al_3Zr$ i.e. β’ which was present in all samples, some indication of $T_1$ precipitates was noticed from SADP of 400 and 800 rpm samples, however these were not observed in images. Incoherent precipitates in two different size ranges: 30–50 nm and 80–140 nm were observed in 400 and 600 rpm samples while none were in 800 rpm sample.

Fig. 6 shows the TEM microstructure of the TMAZ region of the samples processed at various rotation speeds of 400 (Fig. 6a–d), 600 (Fig. 6e–h) and 800 (Fig. 6i–k) rpm. The microstructure is in a partial recovered state as evident by the subgrain structure in the grains (Fig. 6k). The three FSW samples from TMAZ region can be clearly distinguished by the precipitates present in the microstructure. The 400 rpm sample showed presence of GP zones (Fig. 6b) and a few $T_1$ precipitates of 50–85 nm long (Fig. 6a and c). Additionally, many randomly distributed incoherent precipitates, some with circular cross section of ~30–40 nm diameter and length of 30–50 nm and others with lath morphology were also noticed (Fig. 6c and d). These precipitates are likely to be incoherent θ’, β′($Al_3Zr$) and $T_B$ ($Al_7Cu_4Li$) precipitates.

SADP and dark-field images of sample from 600 rpm run show profuse presence of plate shaped precipitates of 30–80 nm length and 3–7 nm thickness in the matrix (Fig. 6e–h). GP zones were absent and

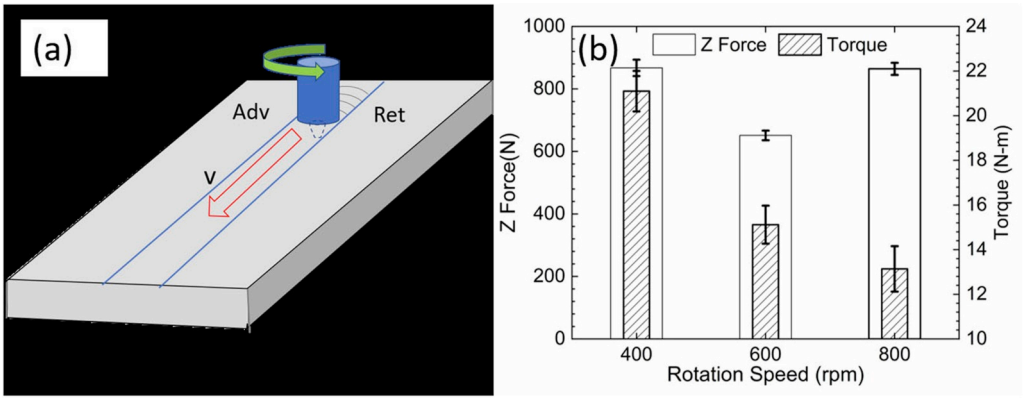


**Fig. 2.** (a) A schematic of the friction stir welding process, (b) bar chart showing axial average force and torque measured during FSW runs of three different rotation speeds.

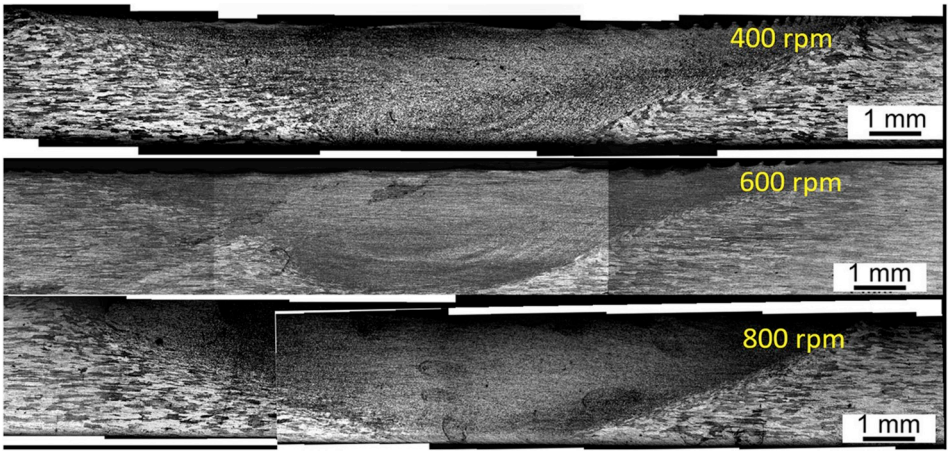


**Fig. 3.** Macrographs of cross-sections of FSW regions of AA2198 alloy samples obtained at three different rotation speeds. Advancing side is on the right hand side.

superlattice spots of β'/θ′ and $T_1$ are clearly present in the SADP. In comparison to the 400 and 600 rpm samples, the 800 rpm sample did not show presence of GP zones, $T_1$ or β' (Fig. 6d). However, many randomly distributed coarse precipitates possibly $T_B$ and/or θ were present in the microstructure.

### 3.2. Thermal stability of FSWAA2198 alloy

DSC thermograms of the samples taken from two different locations of NZ and TMAZ are shown in Fig. 7a and b, respectively. DSC curve of the as-solution treated sample of AA2198 in naturally aged temper is also included for comparison purpose. DSC thermograms are in agreement with the one reported by Decreus et al. [32] on AA2198 and Malard et al. [49] on a similar Al–Cu–Li alloy (AA2050) [48]. Only difference is noted in the low temperature reactions which could possibly be due to the absence of pre-stretch of the alloy used in the present work. Six important peaks are labelled in Fig. 7a. Exothermic peaks 'a' (~120 °C) and 'b' (185 °C) correspond to precipitation of solute nanoclusters/Cu–Mg co-clusters and GP zones respectively [32]. Peak 'c' at ~245 °C corresponds to the precipitation of main strengthening phase $T_1$. Coarsening of $T_1$ phase presents itself as a separate peak in thermogram, this peak is labelled as 'c1' in Fig. 7a. There are two main dissolution events evident in the thermograms: dissolution of clusters and GP or GPB zones in FSW samples at lower temperature (peak 'a1' at

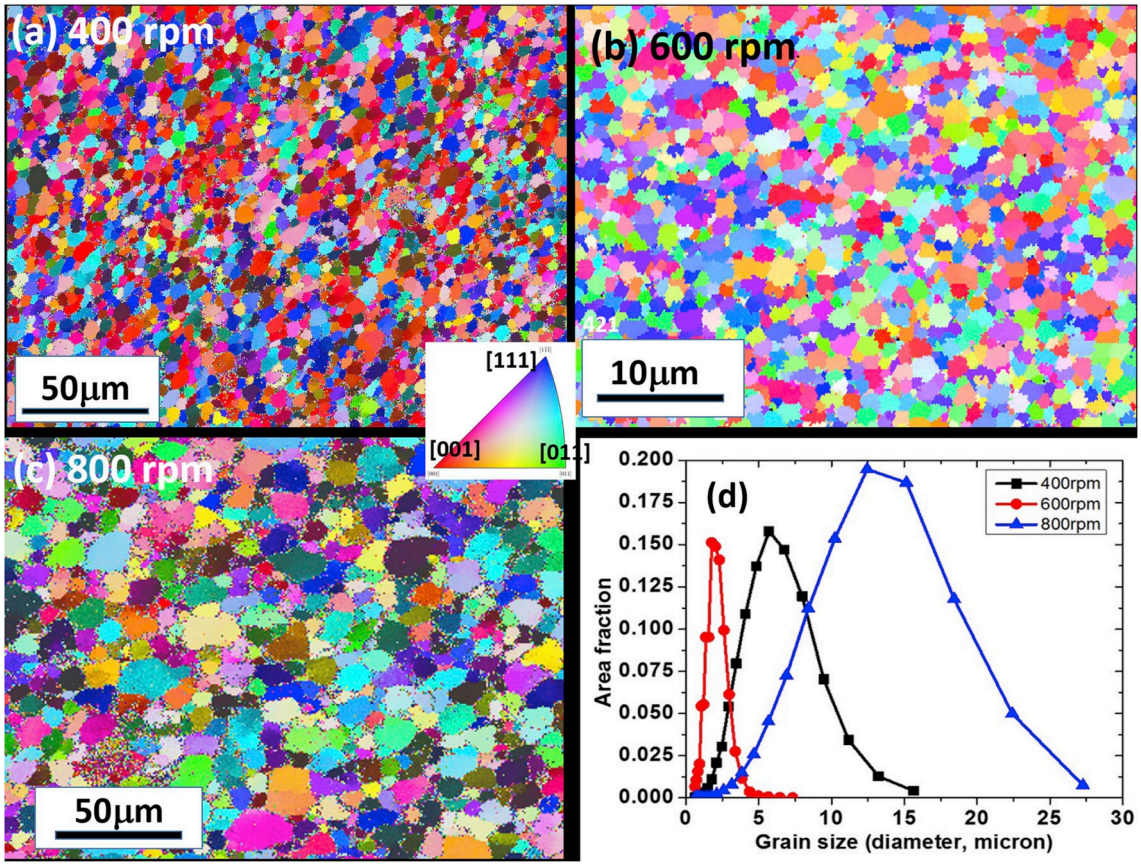


**Fig. 4.** (a) Inverse pole figure (IPF-Z) maps of the nugget zone of the FSW runs with rotation speed of (a) 400 rpm, (b) 600 rpm and (c) 800 rpm, and (d) grain size distribution plots of the NZ location in the FSW samples processed at various rotation speeds. (Z-direction is normal to sheet plane).

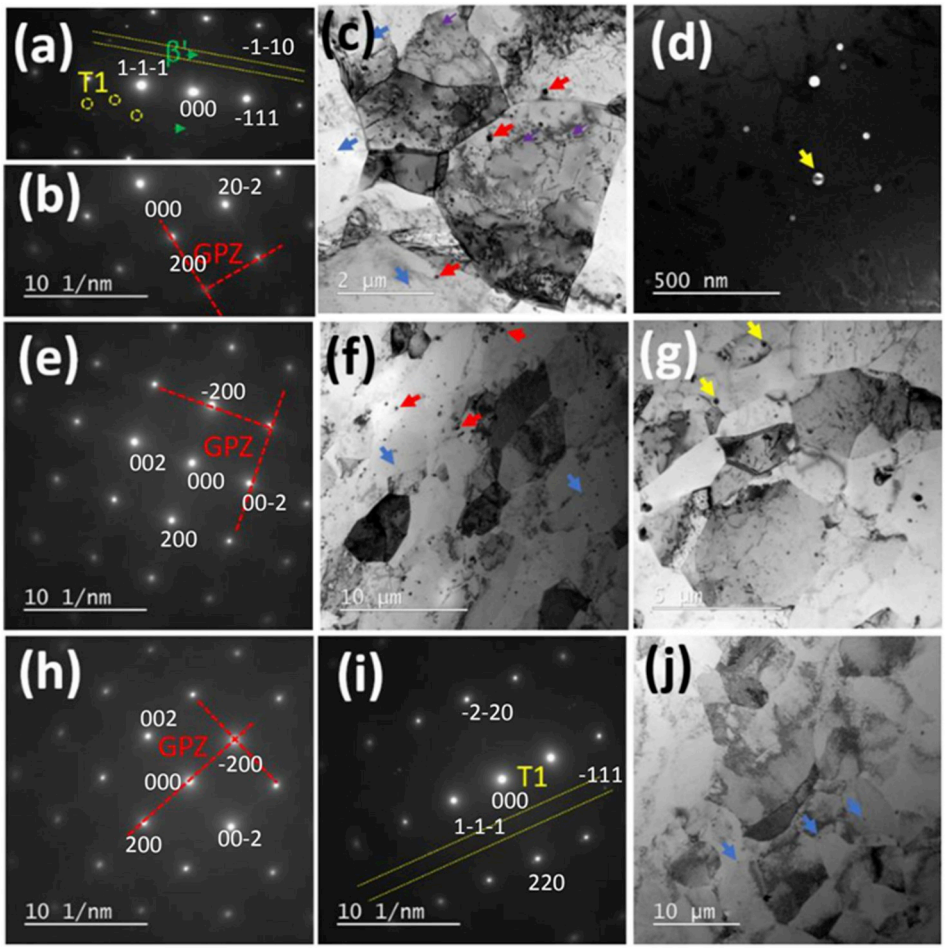


**Fig. 5.** TEM images along with SADPs of NZ region of FSW samples obtained at different rotation speeds of (a–d) 400 rpm, (e–g) 600 rpm and (h–j) 800 rpm. Here, the SADPs zone axis are (a, i) [112] and, (b, e, h) [100], (c, f, g, j) bright-field TEM micrographs and (d)dark field micrograph with [200] g and [100] zone.

140 °C) and a major endothermic peak 'd' starting at around 300 °C in solutionized sample. Dissolution event identified as peak 'd' is a combination of multiple individual endothermic reactions which appear as minor sub-peaks at 325 °C, 365 °C, 410 °C and 450 °C.

### 3.3. Microhardness of FSW AA2198 alloy

Fig. 8 shows 2-dimensional hardness contour maps across the processed zone of the samples obtained at three different rotation speeds. Hardness of the parent metal, which is in T8 temper, is around 170$HV_{0.1}$. Hardness values categorized into four separate ranges: HV < 120, 120 < HV < 140, 140 < HV < 160 and HV > 160. The lower and upper limits of the Vickers hardness are decided on the basis of Vickers hardness of T4 (HV < 120) and T8 (HV > 160) [31]. Intermediate ranges fall within these extremes and correspond to precipitation states in between naturally aged and peak aged tempers.

Subtle differences in the hardness maps with variation in rotation speed are evident. Region with HV < 120 is continuous in 600 and 800 rpm samples, while in 400 rpm run this region is limited to an area corresponding to the outer annular region along the trace of the pin. This also indicates a 'W' shape microhardness profile in 400 rpm run when measured at mid thickness and 'U' shape profile in other samples. This is in contrast to the results of Wang et al. [17] who reported that the hardness profile is U shape at lower rpm which changed to W shape at higher rpm. The U shape hardness profiles were reported by others [43,45,46,57] in Al–Li based alloys.

A notable feature in the 800 rpm sample is the presence of 120–140 HV cap on the low hardness red region (< 120 HV). It could have been formed by the material deforming under shoulder and experiencing a higher temperature as compared to the deeper material around pin.

### 3.4. Uniaxial tensile behaviour

#### 3.4.1. Stress-strain curves

The true stress-plastic strain curves of the samples processed at various rotation speeds are shown in Fig. 9a. For comparison purpose true stress–plastic strain curves of base material in T8 temper and of a T4 sample are also presented in Fig. 9. It is noticed that flow curves of FSW samples lie in between the T4 and T8 curves. Another important observation is the presence of type-A serrations in the FSW tensile curves. The critical strain at which these serrations start increases with the rotation speed. Results of all the tensile tests are listed in Table 1. The yield stress (YS), the ultimate tensile strength (UTS) and ductility values change only marginally with rotation speed of the FSW samples. The FSW samples showed better YS and UTS as compared to T4 temper but elongation to failure was very low and of the order of T8 specimen.

Effect of surface undulations in FSW is revealed by a comparison of the polished and the as-welded 600 rpm tensile curves. As compared to the polished FSW samples, the unpolished specimen (As FSW surface) showed 30 MPa lower YS and significantly lower (1/3rd) uniform elongation. The tensile strength of 600 rpm unpolished sample is 57% of the T8-PA sample which increased to a narrow range of 70–74% in polished samples. The strength of polished samples' is within the range of 60–80% of parent material reported in literature [17,42,43].

According to single parameter strain hardening KME model [52–54] the strain hardening rate can be expressed as:

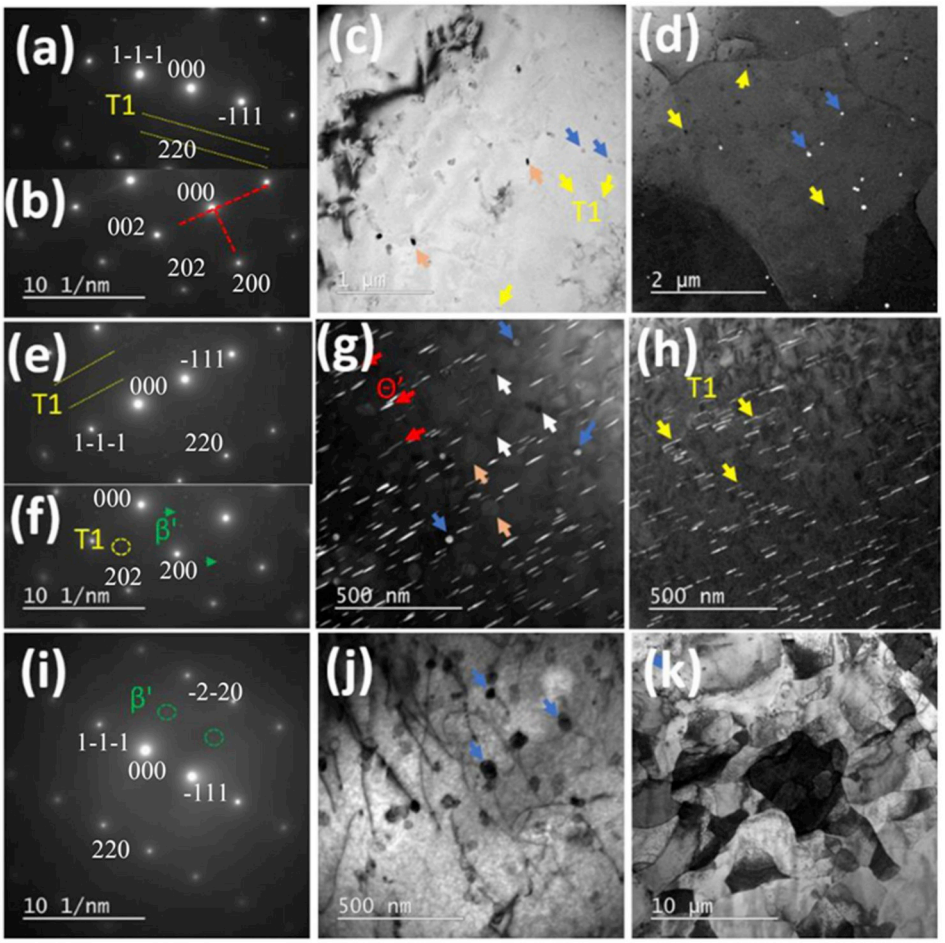


**Fig. 6.** SADP and TEM images of TMAZ region of samples of (a–d) 400, (e–h) 600 and (i–k) 800 rpm runs. Here, the SADP zone axis are: (a, e, i) [112], (b, f) [100] (c, j-k) bright-field TEM micrographs and (d) dark field (DF) image with [200] g and [001] zone, (g) DF with [220] g and [112] zone, (h) DF image with [111] g and [112] zone.

$$\theta = \theta_0 - \beta_0(\sigma - \sigma_y) \tag{1}$$

Here $\sigma_y$ is the yield stress, $\theta$ is instantaneous strain hardening rate $\frac{d\sigma}{d\varepsilon}$, $\theta_0$ is the initial strain hardening rate $\frac{d\sigma}{d\varepsilon}|\sigma = \sigma_y$ and $\sigma_s$ is the saturation stress where strain hardening rate approaches zero. The ratio has been used as the coefficient $\beta_o$ ($=k_2M/2$) in literature [58,59].This is the linear form of the Voce hardening model. Kocks et al. [60,61] showed that this equation can be derived from a single parameter model for forest dislocation density evolution with plastic strain $\varepsilon_p$ :

$$\frac{d\rho}{d\gamma} = k_1\sqrt{\rho} - k_2\rho \tag{2}$$

and Taylor's equation of forest strengthening:

$$\sigma - \sigma_y = \varepsilon Gb\sqrt{\rho} \tag{3}$$

In equation (2) $k_1$ and $k_2$ are dislocation storage and recovery coefficients respectively. α is forest strengthening coefficient with typical value of ~0.3, G is shear modulus with 27 GPa for aluminium, M is Taylor factor with a value of 3.1 for a random textured material and b is burgers vector with magnitude of 2.86 Å. Coefficients in equations (2)

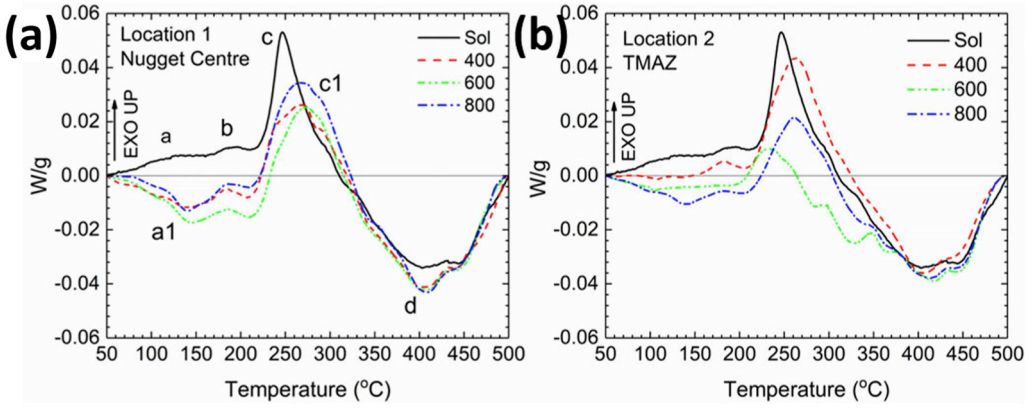


**Fig. 7.** DSC thermograms of samples taken from (a) NZ and (b) TMAZ.

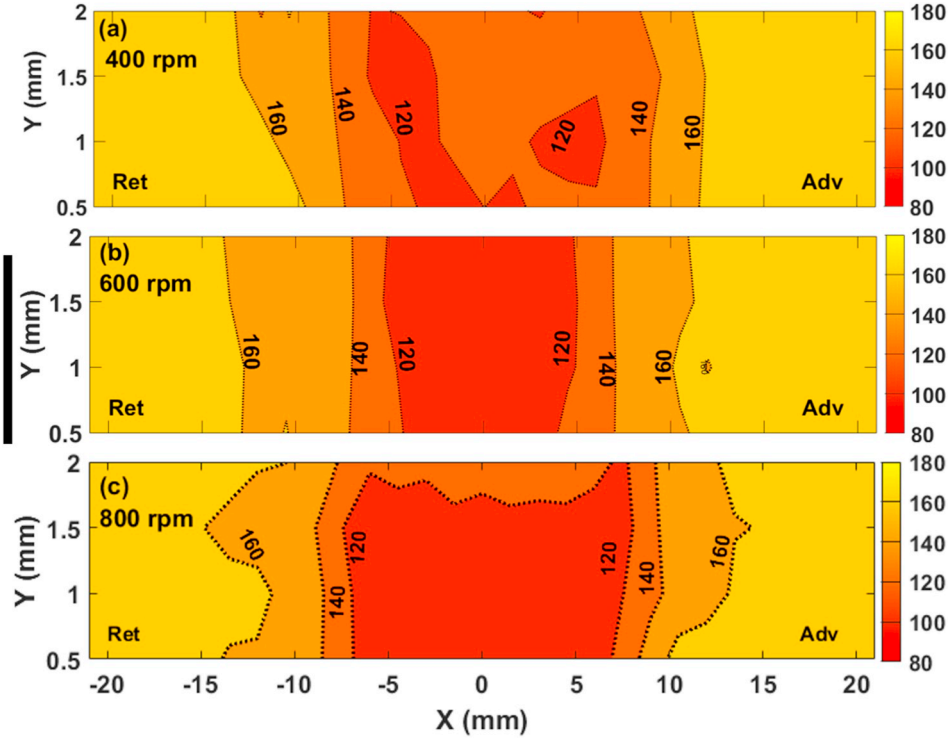


**Fig. 8.** Microhardness maps (on Vickers scale) of the FSW cross-sections.

and (3) are related as –

$k_1 = 2\theta_0/(\alpha GbM^2)$; $k_2 = 2\theta_0/(M^*\sigma_s)$.

Work-hardening behaviour of FSW samples is illustrated in terms of Kocks-Mecking (KM) curve i.e. instantaneous work-hardening rate *vs* reduced flow stress $\sigma = \sigma_y$ plot in Fig. 9b. A linear $\frac{d\sigma}{d\varepsilon}$ *vs.*$\sigma = \sigma_y$ . beha-viour is exhibited by all the samples after an initial deviation. While the initial rapid decrease in the slope of the T4 and T8 curves is due to elastoplastic transition [59], the initial increasing slope of the curve in FSW samples is similar to that observed in overaged aluminium alloys [58,59]. This behaviour is also evident in the tensile curves in Fig. 9a, where an inflection point is present only in FSW samples irrespective of surface preparation. Further, with increasing strain, the work hardening rate decreases linearly with the increase in flow stress as per Voce hardening behaviour.

Voce hardening parameters reveal development of microstructure during deformation of the material. The dislocation storage parameter $k_1$ and recovery parameter $k_2$ of the samples are listed in Table 1. It is noted that range of variation of $k_1$ is limited and the 600 rpm sample had maximum $k_1$ of $6.61 \times 10^8$ $Nm^{-3}$ which is near the value shown by T8 base material. An increasing trend is observed in the recovery parameter $k_2$ with rotation speed of FSW. Lowest rotation speed sample (400 rpm) showed highest saturation stress ($\sigma_s$). This indicates that in the absence of localization of strain the sample will show maximum strain hardening.

### 3.4.2. DIC analysis

The local tensile and strain hardening behaviour of three FSW samples as obtained from DIC analysis are shown in Fig. 10. Each stress-strain plot shows tensile flow behaviour of NZ (red), TMAZ (blue), FSPZ (the complete friction stirred zone, green) and the bulk tensile sample (yellow). Strain hardening plots from NZ, TMAZ and FSPZ are also presented in Fig. 10 with a list of strain hardening parameters. Strain localization within the weld is shown by strain contour maps. It was

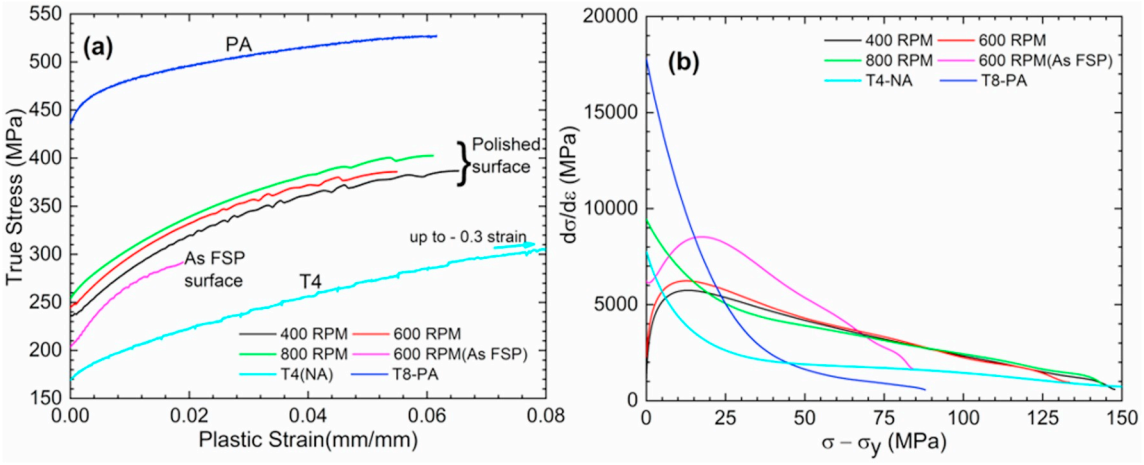


**Fig. 9.** (a) True stress – plastic strain curve of FSW and base material and (b) strain hardening rate curves calculated from the data in (a).

**Table 1**
Summary of tensile test results and strain hardening parameters.

| | Base material (AA2198) | | As FSW | Polished samples | | |
|---|---|---|---|---|---|---|
| | T4 | T8 | 600 | 400 | 600 | 800 |
| Yield strength (MPa) | 169 ± 4 | 433 ± 3 | 207 ± 2 | 233 ± 21 | 247 ± 4 | 248 ± 1 |
| UTS (MPa) | 326 ± 4 | 494 ± 3 | 284 ± 2 | 351 ± 5 | 361 ± 3 | 365 ± 1 |
| Elongation (%) | 37 ± 4 | 11 ± 1 | 3.5 ± 1.0 | 9.5 ± 2.0 | 8.9 ± 1.0 | 10 ± 1.0 |
| $k_1$ ($Nm^{-3}$) × $10^8$ | 5.11 × $10^8$ | 6.49 × $10^8$ | 9.52 × $10^8$ | 5.88 × $10^8$ | 6.61 × $10^8$ | 5.99 × $10^8$ |
| $k_2$ ($Nm^{-4}$) | 38 | 79 | 61 | 25 | 33 | 36 |
| $\sigma_s$ (MPa) | 94 | 57 | 110 | 160 | 138 | 115 |

noticed that the entire strain during tensile deformation was constrained only within the FSPZ in all three samples, but its distribution differs with rotation speed. Thus, FSPZ behaviour is more representative of the weld behaviour than macro-tensile behaviour.

Tensile properties calculated from the local stress-strain plots are listed in Table 2. It is noted that there is no significant difference in yield strengths of NZ and TMAZ but these two zones show different strain hardening behaviours. Local yield strength increased with increasing rotation speed, with 800 rpm showing ~248 MPa local YS and maximum flow stress (MFS) of ~404 MPa. Similar to bulk tensile behaviour, serrations were also observed in local stress-strain curves. The YS values in all cases are higher than T4 temper but much lower than

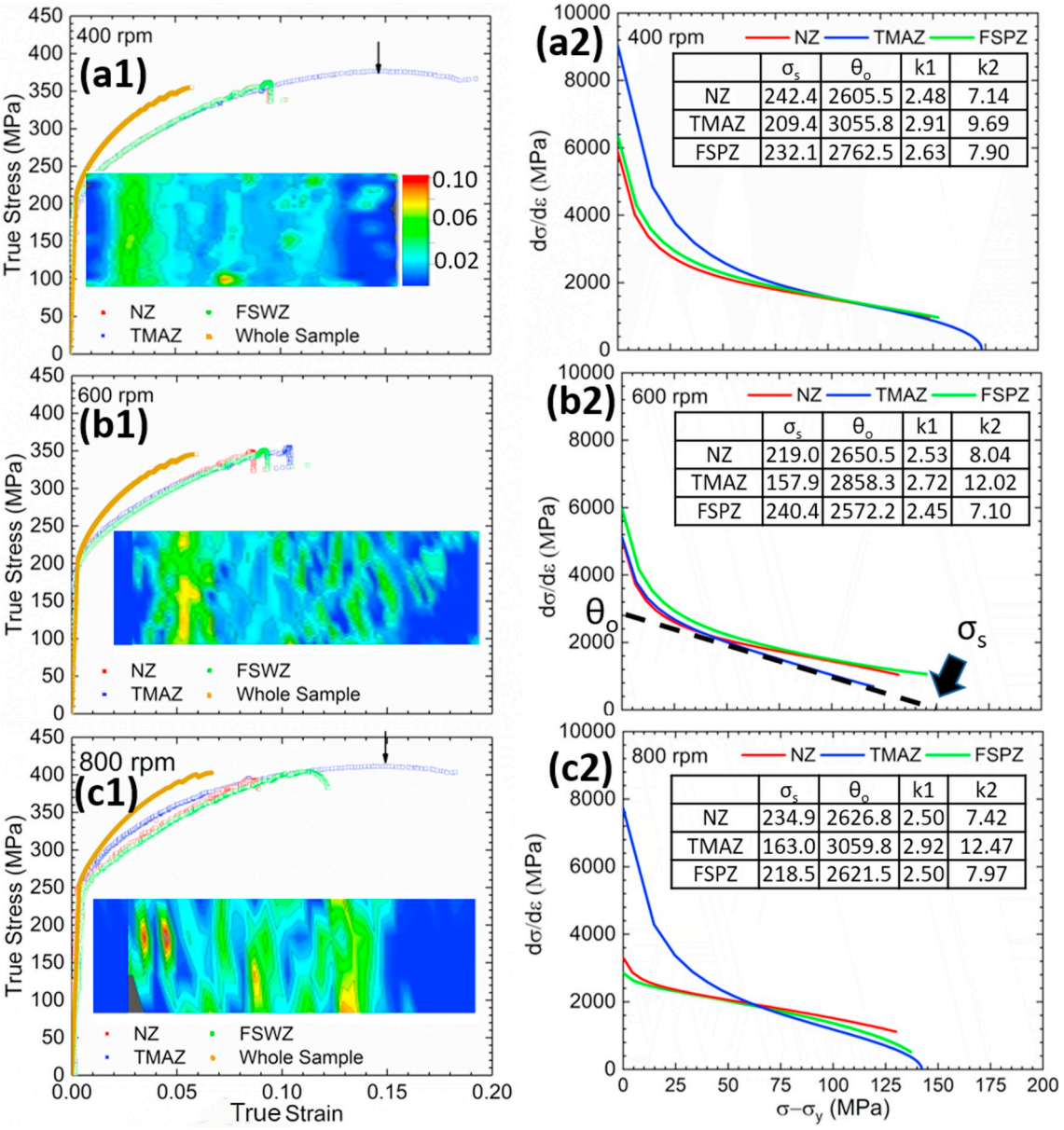


**Fig. 10.** Local stress-strain curves (a1-c1) and Kocks-Mecking plots (a2-c2) from the three locations in FSW samples processed at (a) 400, (b) 600 and (c) 800 rpm rotation speed. $k_1$ values are in the multiple of $10^8$.

**Table 2**
Local strength and elongation values calculated from DIC analysis.

| | 400 rpm | | | 600 rpm | | | 800 rpm | | |
|---|---|---|---|---|---|---|---|---|---|
| | NZ | TMAZ | FSPZ | NZ | TMAZ | FSPZ | NZ | TMAZ | FSPZ |
| YS (MPa) | 212 | 204 | 210 | 214 | 232 | 224 | 247 | 250 | 248 |
| MFS (MPa) | 362 | 376 | 362 | 349 | 260 | 351 | 393 | 411 | 405 |
| El(%) | 9.7 | 17 | 9.6 | 8.7 | 8.7 | 10 | 8.9 | 18 | 12 |

T8 temper. Elongation (El%) values also fall between the T4 and T8 tempers.

Strain hardening parameters were calculated by fitting a straight line to the linear portion of K-M curve as shown in Fig. 10(b2). NZ and TMAZ regions showed similar strain hardening behaviour only in 600 rpm sample. The strain distribution across weld was also more uniform (Fig. 10(a1)). This unique behaviour of 600 rpm sample is consistent with the different microstructure in this sample as shown in previous sections.

### *3.4.3. 3Fractography*

Wang et al. [17] have categorized the failure mode into three different modes based on location of the failure: Mode I, II, and III. Failure occurs in the SZ, HAZ and at the border of TMAZ and SZ in Mode I, II and III respectively. According to this terminology fracture in present work occurred by Mode III from TMAZ region. Fig. 11 shows secondary electron micrographs of fracture surfaces of the failed tensile specimens processed at 600 rpm. Three points are noticed:1) fracture is fibrous in nature, 2) fracture is heterogeneous in nature (as in Fig. 11b) where some areas show profuse dimples (red circle) and other regions flat surface and 3) presence of round (red arrow), rod and plate shaped particles (green arrows) inside the dimples (Fig. 11c). Thus, crack seem to originate by particle matrix interface de-cohesion at coarse $T_B$ or θ' particles distributed along grain boundaries. These small voids coalesce with further straining along grain boundaries and the cracks propagating in an intragranular manner into the grain interior creating flat surfaces in between highly dimpled grain boundary regions.

## 4. Discussion

FSW, like any other welding method causes heterogeneous microstructure across the weld seam. However, the extent of heterogeneity and local microstructures depend on the local thermo-mechanical history. A quantitative estimate of heat generation at different rotation speeds can be obtained by the heat input per unit length during FSW and it is defined as:

$$P = (\text{Torque} \times 2 \times \pi \times \text{rpm})/(\text{traverse speed in mm/min}) \quad (4)$$

This results in 264, 283, 327 J/mm heat input per mm for 400, 600 and 800 rpm respectively. Thus, temperatures in higher rpm runs must exceed those in lower rpm runs as predicted by various heat evolution models of FSW [62]. This difference in thermal profiles in different runs gets displayed in Z-force and torque values while heterogeneity within a run is evidenced by local properties as contours in microhardness maps, microstructures, DSC and DIC analysis. Following salient points can be summarised from the results section:

1) Strength and ductility of FSW samples were independent of rotation speed even though local microstructure and mechanical behavior were different.
2) Yield stress of NZ, TMAZ and the weld zone increased with increase in rotation speed.
3) Tensile curves for all the FSW samples showed type-A serrations. Serrations were also noticed in local DIC curves. The critical strain at which serrations start increased with rotation speed.
4) The region with microhardness values less than T4 temper, i.e. < 120 HV, increased in area with rotation speed, indicating a wider soft area at center of the weld.
5) TEM results indicate increase in precipitates dissolution and increased presence of GP zones at NZ with rotation speed. At TMAZ only 600 rpm sample showed significant presence of $T_1$ and θ'. GP zones were present only in 400 rpm sample along with very few $T_1$ plates. At TMAZ, only incoherent coarse precipitates were observed in 800 samples.
6) DSC and TEM results also showed presence of only clusters and GP zones along with coarse precipitates in weld nugget samples. Clusters content increased with rotation speed of FSW.
7) The 600 rpm sample was peculiar in the sense that TMAZ of only this run showed significant distribution of $T_1$ precipitate in the matrix. The FSW nugget of this run also showed finest grain size while all other samples showed coarse precipitates along with clusters and in some cases GP1 zones. Strain hardening behavior of this sample was also different than other two runs.
8) The 600 rpm sample also showed lowest saturation stress, $\sigma_s$ and highest recovery parameter $k_2$ of NZ and TMAZ.
9) FSW samples showed poor ductility due to localization of strain in NZ and TMAZ. When the strain is calculated based on deformation zone only (FSPZ), true ductility was significantly higher ($\varepsilon_p \sim 0.10$ to 0.15) than base metal ($\varepsilon_p \sim 0.06$).

### *4.1. Microstructure evolution during FSW*

AA2198 alloy in T8 temper is strengthened primarily by $T_1$ precipitates which are semi-coherent with α matrix and form on the {111} habit plane. Apart from $T_1$, GPI/II zones and θ' are also reported by Deschamps et al. [28] in peak aged temper. FSW imparts thermal input along with high strains at high strain rates which change the microstructure of the base metal in short duration. Deformation at elevated temperature enhances the diffusion and thus, the kinetics of coarsening and dissolution in the NZ and TMAZ. For given process parameters, the peak temperature and the rate of heating or cooling depend on location of the material with respect to seam with NZ experiencing highest temperatures and faster rates. During the initial heating ramp the $T_1$ precipitates present in the material get coarsen and then dissolve when

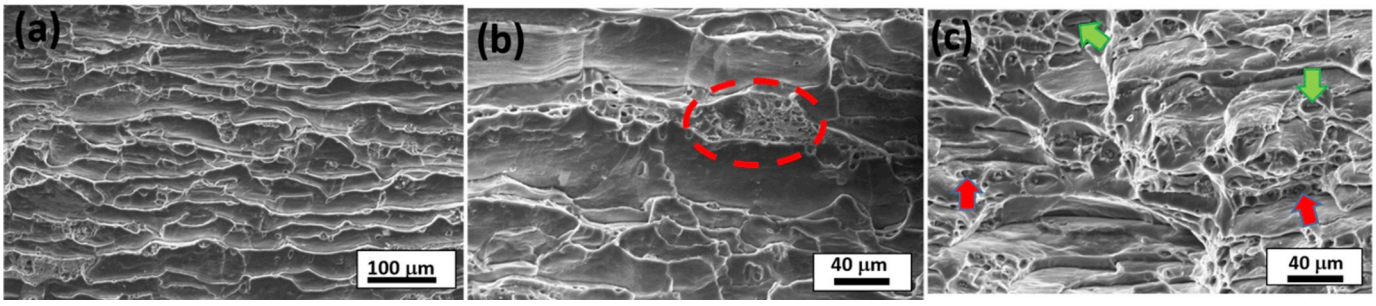


**Fig. 11.** Fractographs of the failed FSW 600 rpm tensile specimen at three different magnifications.

local temperature exceeds $T_1$ solvus (> 300 °C). Dissolution stops when local temperature drops below the solvus during cooling ramp. The solutes present in the matrix as a result of reversion then again continue precipitation reaction. Some precipitation of $T_1$ or GP zones can also occur at lower temperatures in the intermediate region between coarse precipitates. The coarsening reaction stops at room temperature due to reduction in mobility of solute atoms. In the absence of supersaturated vacancies, natural aging after welding is unlikely to happen.

NZ experiences highest peak temperatures above precipitates' solvus and as a result dissolution of precipitates occurs. Higher temperature at higher rotation speeds of FSW thus, led to higher cluster content in the nugget and wider < 120 HV microhardness region (Fig. 8). TEM images showed the NZ grains to be fully recrystallized with very few scattered dislocations. It is well known that stacking faults are the primary locations for $T_1$ nucleation and in the absence of dislocations, $T_1$ precipitation is suppressed while that of Al–Cu–Mg ternary system precipitates GP zones and θ' is enhanced. Thus, the nugget zones in all the FSW samples consist of solid solution, coarse precipitates, solute clusters and GP zones with absence of $T_1$ precipitates.

The TMAZ is exposed to reduced peak temperature as compared to NZ which results in a different microstructure. The TMAZ by definition does not recrystallize completely due to lower plastic deformation and lower peak temperature. All TEM specimens from TMAZ showed dislocation structures. Presence of dislocations facilitates $T_1$ precipitation. It is evident from TEM images that GP zones and very small fraction of $T_1$ along with coarse $T_B$ and/or θ precipitates were present at TMAZ of 400 rpm sample. This could be due to limited dissolution during FSW owing to low peak temperatures. The available solutes could only form GP zones and a small number of $T_1$ and θ′ precipitates. In the 600 rpm sample, with higher peak temperature, relatively higher reversion occurred which resulted in significant precipitation of $T_1$ and θ' precipitates (Fig. 5e and f). Relatively higher local temperatures at 800 rpm caused coarsening of the re-precipitated $T_1$ to $T_B$ and also coarsening of θ precipitates which were predominantly observed at TMAZ of 800 rpm sample.

### 4.2. Weld strength

Friction stir welding and processing can produce a nonuniform thickness across the processed zone due to shoulder digging. However, the tensile tests of FSW transverse specimens, thus do not reveal the true mechanical response of microstructure but a combined geometrical and microstructural effect. Thus, low thickness at nugget zone significantly localize the strain during a tensile test which can lead to poor ductility and strength in unpolished sample. Microhardness maps showed that the nugget zone is the weakest area of the weld. This is particularly true for 'U' shaped microhardness profile. In such cases the combination of poor strength and reduced thickness culminate into catastrophic combination adversely affecting joint properties.

The independence of FSW joint strength on process parameters is not surprising. As mentioned earlier a transverse tensile specimen of a friction stir weld can be considered as a composite where materials with different microstructures and strength, i.e., base metal (BM), HAZ, TMAZ, and NZ are connected in series. Different zones have different resistances to deformation due to differences in grain size, precipitate kind, their size and distribution. Microhardness maps show that only the width of these different zones is changed in different FSW samples not the material elements. Thus, always the weakest link of this chain will carry the load and deform until it strain-hardens and next region starts deforming. But it can have an effect on overall ductility and strain hardening behaviour. However, it is marginal in the present work.

### 4.3. Strain hardening behavior

#### 4.3.1. Bulk behavior

As discussed in results section all three polished transverse FSW samples and the one as-FSW sample showed an inflection point just after yielding in stress-strain curve (Fig. 9a) similar to the typical curve obtained for overaged aluminium alloys [59,60]. Except 800 rpm sample all others show a hump in the KM curves (Fig. 9b). As stated earlier, deformation during tensile test is most likely to start at the NZ which has lowest strength (Fig. 10). DSC and TEM results confirmed the presence of coarse precipitates indicating overaging of precipitates during FSW. However, when local stress-strain curves are considered the above explanation does not hold. None of the local stress-strain or KM curves show the behaviour observed in bulk specimen. Thus, it seems that the inflection point and the associated KM curve are due to the inhomogeneous deformation in the weld zone. Initial yield during the tensile deformation starts at location having lowest strength, for example, in 400 rpm sample it can start at TMAZ with YS of 206 MPa. With further extension this location strain hardens, and further straining can be shifted to other locations. Microstructural heterogeneity as a function of location can to lead to differences in strain hardening behaviour as clearly depicted by local KM curves shown in Fig. 10b. This change in the region undergoing localized deformation and not coarse precipitates thus, seems to be the cause of the inflection in bulk stress-strain curves. It is, therefore, imperative that uniaxial tensile behaviour of macro specimen cannot be directly interpreted in terms of microstructure because these curves are composite of local tensile behaviours.

#### 4.3.2. Local behaviour

Strain hardening behaviour of NZ and TMAZ was different in all the samples, however there were some differences with rotation speeds. All TMAZs show a steep drop in KM curve as compared to NZ. It is quantified in $k_2$ (or β) values, which are relatively higher for TMAZ than for NZ. As dynamic recovery in stage III of the strain hardening is attributed to cross slip of dislocations, it will be affected by the solutes present in the matrix. Cu and Mg atoms in solution can reduce the stacking fault energy (SFE) of the matrix thus making the glide of screw segments of dislocations onto the cross-slip plane difficult, thereby suppressing dislocation annihilation. Since $k_2$ values at TMAZ increase with rotation speed, it appears that solute in the matrix decreases at higher rotation speeds, thus increasing the recovery rate. This is consistent with the DSC results (Fig. 7) where exothermic reactions were noticed at TMAZ of 400 rpm sample while increasing endothermic heat evolution of cluster dissolution was observed with increasing the rotation speed. With increasing rotation speed more solutes can combine to form clusters and as a result less solute is available in the matrix to have a substantial effect on SFE of Al. Recovery rate of nugget zone was relatively lower than TMAZ which suggests higher solutes in the solution but DSC thermograms show only endothermic reaction at low temperatures indicating presence of clusters and not solutes. Presence of 'a1' peak however, shows that solutes are still present in the matrix which take part in GPZ precipitation reaction. Higher recovery at TMAZ leads to faster strain hardening rate drop and cause strain localization. Higher strain at TMAZ (> 0.18) as compared to NZ (< 0.10) in stress-strain curves in Fig. 10a and c are indicative of this.

The parameter $k_1$ is an indicative of dislocation storage capability of the microstructure and is slightly higher at TMAZ owing to larger volume fraction of coarse precipitates. The exothermic heat evolution during DSC in peak 'c' and 'c1' is less for TMAZ samples which suggests higher volume fraction of precipitates at TMAZ.

The local work hardening rate ($\theta_o$) and saturation stress ($\sigma_s$) values fall into the same range: 2000–4000 MPa and 50–350 MPa respectively, as reported by Deschamps et al. [28] in AA2198 aged to different tempers. The $\theta_o$ values are higher and $\sigma_s$ values are lower in TMAZ of all samples suggesting low strain hardening ability at TMAZ. The ductility values are thus counterintuitive where TMAZ in all samples showed significantly higher elongation. In this respect it should be kept in mind that NZ did not undergo necking and failure. It did not deform further than the reported elongation while the TMAZ, which has lower strain

hardening ability, underwent strain localization through necking. The initiation of necking in TMAZ stress-strain plot is marked by a vertical arrow in Fig. 10(a1) and (c1).

Local initial strain hardening rate is always higher than that of pure Al i.e. G/20 (1350 MPa). The strain hardening behaviour of whole FSP zone is closer to that of NZ, which belongs to centre of the nugget. This is true for all three samples. The strain hardening parameters listed in Fig. 10b for the NZ and FSPZ are also similar. This indicates that most of deformation during tensile testing is occurring at the middle of the nugget and the strain hardening behaviour is dominated by it. The $\theta_o$ values of NZ are all above that of pure Al (1350 MPa) indicating better dislocation storage.

## 5. Conclusions

The effect of tool rotation speed in the range of 400–800 rpm during FSW of AA2198 alloy on microstructure and bulk as well as local mechanical properties were investigated. It was brought out from this study that even though macroscale mechanical properties indicate no significant effect of tool rotation speed on the joint strength, there is a notable effect on local mechanical properties. These local differences can be directly related to the differences in microstructure across weld cross-section. It was noted that the yield strength of nugget zone and thermo-mechanically affected zone increased with increasing the rotation speed of FSW. Out of the different regions of the weld, TMAZ undergoes high dynamic recovery leading to fast drop in strain hardening ability. This results in strain localization, which subsequently causes commonly observed failure in this region.

## Declaration of competing interest

None.

## Acknowledgements

MY and NPG would like to thank space technology cell (STC), IIT Kanpur for providing funding for the present work. We would also like to acknowledge Mr. Shivam Trivedi and mechanical testing laboratory, IIT Kanpur for carrying out microhardness and tensile tests. NN and SVSNM would like to thank Director, ISRO for permission to publish this work.

## Appendix A. Supplementary data

Supplementary data to this article can be found online at https://doi.org/10.1016/j.matchar.2019.110002.

## Potential competing interests

Do not exist.

## Data availability

The raw/processed data required to reproduce these findings cannot be shared at this time as the data also forms part of an ongoing study.

## References

[1] N.E. Prasad, A.A. Gokhale, R. Wanhill, Aluminium–lithium Alloys, Aerospace Materials and Material Technologies, Springer, 2017, pp. 53–72.
[2] J. Yan, M. Gao, G. Li, C. Zhang, X. Zeng, M. Jiang, Microstructure and mechanical properties of laser-MIG hybrid welding of 1420 Al-Li alloy, Int. J. Adv. Manuf. Technol. 66 (2013) 1467–1473.
[3] G.J. Ram, T. Mitra, M. Raju, S. Sundaresan, Use of inoculants to refine weld solidification structure and improve weldability in type 2090 Al- Li alloy, Mater. Sci. Eng. A 276 (2000) 48–57.
[4] X. Zhang, W. Yang, R. Xiao, Microstructure and mechanical properties of laser beam welded Al–Li alloy 2060 with Al–Mg filler wire, Mater. Des. 88 (2015) 446–450.
[5] W. Thomas, Friction stir welding, International Patent Application No. PCT/GB92/02203 and GB Patent Application No. 9125978.8, vol. 460, US Patent, 1991, p. 317.
[6] R.S. Mishra, Z. Ma, Friction stir welding and processing, Mater. Sci. Eng. R Rep. 50 (2005) 1–78.
[7] M.W. Mahoney, R.S. Mishra, Friction Stir Welding and Processing, ASM International, 2007.
[8] H.-H. Cho, H.N. Han, S.-T. Hong, J.-H. Park, Y.-J. Kwon, S.-H. Kim, R.J. Steel, Microstructural analysis of friction stir welded ferritic stainless steel, Mater. Sci. Eng. A 528 (2011) 2889–2894.
[9] H. Kokawa, S. Park, Y. Sato, K. Okamoto, S. Hirano, M. Inagaki, Microstructures in friction stir welded 304 austenitic stainless steel, Weld. World 49 (2005) 34–40.
[10] G. Guo, Y. Shen, Friction stir welding of dissimilar stainless steels: evaluation of flow pattern, microstructure and mechanical properties, Mater. Res. Express 6 (2019) 056510.
[11] R. Ramesh, I. Dinaharan, R. Kumar, E. Akinlabi, Microstructure and mechanical characterization of friction-stir-welded 316L austenitic stainless steels, J. Mater. Eng. Perform. 28 (2019) 498–511.
[12] P. Cavaliere, M. Cabibbo, F. Panella, A. Squillace, 2198 Al–Li plates joined by friction stir welding: mechanical and microstructural behavior, Mater. Des. 30 (2009) 3622–3631.
[13] A. Steuwer, M. Dumont, J. Altenkirch, S. Birosca, A. Deschamps, P. Prangnell, P. Withers, A combined approach to microstructure mapping of an Al–Li AA2199 friction stir weld, Acta Mater. 59 (2011) 3002–3011.
[14] O. Hatamleh, A comprehensive investigation on the effects of laser and shot peening on fatigue crack growth in friction stir welded AA 2195 joints, Int. J. Fatigue 31 (2009) 974–988.
[15] H. Sidhar, R.S. Mishra, Aging kinetics of friction stir welded Al-Cu-Li-Mg-Ag and Al-Cu-Li-Mg alloys, Mater. Des. 110 (2016) 60–71.
[16] H. Liu, Y. Hu, C. Dou, D.P. Sekulic, An effect of the rotation speed on microstructure and mechanical properties of the friction stir welded 2060-T8 Al-Li alloy, Mater. Char. 123 (2017) 9–19.
[17] F. Wang, W. Li, J. Shen, S. Hu, J. dos Santos, Effect of tool rotational speed on the microstructure and mechanical properties of bobbin tool friction stir welding of Al–Li alloy, Mater. Des. 86 (2015) 933–940.
[18] J. Zhang, X. Feng, J. Gao, H. Huang, Z. Ma, L. Guo, Effects of welding parameters and post-heat treatment on mechanical properties of friction stir welded AA2195-T8 Al-Li alloy, J. Mater. Sci. Technol. 34 (2018) 219–227.
[19] C. Bitondo, U. Prisco, A. Squillace, G. Giorleo, P. Buonadonna, G. Dionoro, G. Campanile, Friction stir welding of AA2198-T3 butt joints for aeronautical applications, Int. J. Material Form. 3 (2010) 1079–1082.
[20] P. Threadgill, A. Leonard, H. Shercliff, P. Withers, Friction stir welding of aluminium alloys, Int. Mater. Rev. 54 (2009) 49–93.
[21] P. Cavaliere, R. Nobile, F. Panella, A. Squillace, Mechanical and microstructural behaviour of 2024–7075 aluminium alloy sheets joined by friction stir welding, Int. J. Mach. Tool Manuf. 46 (2006) 588–594.
[22] G. Liu, L. Murr, C. Niou, J. McClure, F. Vega, Microstructural aspects of the friction-stir welding of 6061-T6 aluminum, Scr. Mater. 37 (1997) 355–361.
[23] J. Ouyang, E. Yarrapareddy, R. Kovacevic, Microstructural evolution in the friction stir welded 6061 aluminum alloy (T6-temper condition) to copper, J. Mater. Process. Technol. 172 (2006) 110–122.
[24] M.A. Sutton, B. Yang, A.P. Reynolds, R. Taylor, Microstructural studies of friction stir welds in 2024-T3 aluminum, Mater. Sci. Eng. A 323 (2002) 160–166.
[25] V. Araullo-Peters, B. Gault, F. De Geuser, A. Deschamps, J.M. Cairney, Microstructural evolution during ageing of Al–Cu–Li–x alloys, Acta Mater. 66 (2014) 199–208.
[26] T. Dorin, A. Deschamps, F. De Geuser, C. Sigli, Quantification and modelling of the microstructure/strength relationship by tailoring the morphological parameters of the T1 phase in an Al–Cu–Li alloy, Acta Mater. 75 (2014) 134–146.
[27] T. Dorin, F. De Geuser, W. Lefebvre, C. Sigli, A. Deschamps, Strengthening mechanisms of T1 precipitates and their influence on the plasticity of an Al–Cu–Li alloy, Mater. Sci. Eng. A 605 (2014) 119–126.
[28] A. Deschamps, B. Decreus, F. De Geuser, T. Dorin, M. Weyland, The influence of precipitation on plastic deformation of Al–Cu–Li alloys, Acta Mater. 61 (2013) 4010–4021.
[29] M. Knüwer, J. Schumacher, H. Ribes, F. Eberl, B. Bes, 2198-Advanced Aluminium-Lithium Alloy for A350 Skin Sheet Application, Presentation for the 17th AeroMat Conference & Exposition, Seattle, USA, 2006, pp. 1–27.
[30] N.D. Alexopoulos, E. Migklis, A. Stylianos, D.P. Myriounis, Fatigue behavior of the aeronautical Al–Li (2198) aluminum alloy under constant amplitude loading, Int. J. Fatigue 56 (2013) 95–105.
[31] B. Decreus, A. Deschamps, F. de Geuser, C. Sigli, Influence of natural ageing and deformation on precipitation in an Al–C u–L i alloy, Adv. Eng. Mater. 15 (2013) 1082–1085.
[32] B. Decreus, A. Deschamps, F. De Geuser, P. Donnadieu, C. Sigli, M. Weyland, The influence of Cu/Li ratio on precipitation in Al–Cu–Li–x alloys, Acta Mater. 61 (2013) 2207–2218.
[33] R.S. Mishra, H. Sidhar, Friction Stir Welding of 2xxx Aluminum Alloys Including Al-Li Alloys, Butterworth-Heinemann, 2016.
[34] C. Gao, Z. Zhu, J. Han, H. Li, Correlation of microstructure and mechanical properties in friction stir welded 2198-T8 Al–Li alloy, Mater. Sci. Eng. A 639 (2015) 489–499.
[35] M.M. Khalilabad, Y. Zedan, D. Texier, M. Jahazi, P. Bocher, Effect of tool geometry and welding speed on mechanical properties of dissimilar AA2198–AA2024 FSWed joint, J. Manuf. Process. 34 (2018) 86–95.
[36] Y.E. Ma, Z. Xia, R. Jiang, W. Li, Effect of welding parameters on mechanical and fatigue properties of friction stir welded 2198 T8 aluminum–lithium alloy joints,

Eng. Fract. Mech. 114 (2013) 1–11.
[37] B. Gibson, M. Ballun, G. Cook, A. Strauss, Friction stir lap joining of 2198 aluminum–lithium alloy with weaving and pulsing variants, J. Manuf. Process. 18 (2015) 12–22.
[38] Y.E. Ma, Z. Zhao, B. Liu, W. Li, Mechanical properties and fatigue crack growth rates in friction stir welded nugget of 2198-T8 Al–Li alloy joints, Mater. Sci. Eng. A 569 (2013) 41–47.
[39] C. Gao, Y. Ma, L.-z. Tang, P. Wang, X. Zhang, Microstructural evolution and mechanical behavior of friction spot welded 2198-T8 Al-Li alloy during aging treatment, Mater. Des. 115 (2017) 224–230.
[40] Y. Tao, D. Ni, B. Xiao, Z. Ma, W. Wu, R. Zhang, Y. Zeng, Origin of unusual fracture in stirred zone for friction stir welded 2198-T8 Al-Li alloy joints, Mater. Sci. Eng. A 693 (2017) 1–13.
[41] M. Reimann, J. Goebel, T.M. Gartner, J.F. dos Santos, Refilling termination hole in AA 2198–T851 by refill friction stir spot welding, J. Mater. Process. Technol. 245 (2017) 157–166.
[42] T. Le Jolu, T.F. Morgeneyer, A. Denquin, M. Sennour, A. Laurent, J. Besson, A.-F. Gourgues-Lorenzon, Microstructural characterization of internal welding defects and their effect on the tensile behavior of FSW joints of AA2198 Al-Cu-Li alloy, Metall. Mater. Trans. A 45 (2014) 5531–5544.
[43] W. Li, R. Jiang, Z. Zhang, Y.E. Ma, Effect of rotation speed to welding speed ratio on microstructure and mechanical behavior of friction stir welded aluminum–L ithium alloy joints, Adv. Eng. Mater. 15 (2013) 1051–1058.
[44] T. Le Jolu, T.F. Morgeneyer, A. Denquin, A.-F. Gourgues-Lorenzon, Fatigue lifetime and tearing resistance of AA2198 Al–Cu–Li alloy friction stir welds: effect of defects, Int. J. Fatigue 70 (2015) 463–472.
[45] A. Shukla, W. Baeslack Iii, Study of microstructural evolution in friction-stir welded thin-sheet Al–Cu–Li alloy using transmission-electron microscopy, Scr. Mater. 56 (2007) 513–516.
[46] J. Schneider, A. Nunes, P. Chen, G. Steele, TEM study of the FSW nugget in AA2195-T81, J. Mater. Sci. 40 (2005) 4341–4345.
[47] Y. Lin, Z. Zheng, Microstructural evolution of 2099 AlLi alloy during friction stir welding process, Mater. Char. 123 (2017) 307–314.
[48] B. Malard, F. De Geuser, A. Deschamps, Microstructure distribution in an AA2050 T34 friction stir weld and its evolution during post-welding heat treatment, Acta Mater. 101 (2015) 90–100.
[49] O. Hatamleh, J. Lyons, R. Forman, Laser and shot peening effects on fatigue crack growth in friction stir welded 7075-T7351 aluminum alloy joints, Int. J. Fatigue 29 (2007) 421–434.
[50] C. Leitão, I. Galvão, R. Leal, D. Rodrigues, Determination of local constitutive properties of aluminium friction stir welds using digital image correlation, Mater. Des. 33 (2012) 69–74.
[51] W.D. Lockwood, B. Tomaz, A.P. Reynolds, Mechanical response of friction stir welded AA2024: experiment and modeling, Mater. Sci. Eng. A 323 (2002) 348–353.
[52] W. Lockwood, A.P. Reynolds, Simulation of the global response of a friction stir weld using local constitutive behavior, Mater. Sci. Eng. A 339 (2003) 35–42.
[53] C. Genevois, A. Deschamps, P. Vacher, Comparative study on local and global mechanical properties of 2024 T351, 2024 T6 and 5251 O friction stir welds, Mater. Sci. Eng. A 415 (2006) 162–170.
[54] A. Reynolds, F. Duvall, Digital image correlation for determination of weld and base metal constitutive behavior, Weld. J. N. Y. 78 (1999) 355–s.
[55] E. Gmelin, S. St M, Calibration of differential scanning calorimeters, Pure Appl. Chem. 67 (1995) 1789–1800.
[56] G. Höhne, W. Hemminger, H.-J. Flammersheim, Calibration of Differential Scanning Calorimeters, Differential Scanning Calorimetry, Springer, 2003, pp. 65–114.
[57] A. Shukla, W. Baeslack, Study of process/structure/property relationships in friction stir welded thin sheet Al–Cu–Li alloy, Sci. Technol. Weld. Join. 14 (2009) 376–387.
[58] A. Simar, Y. Bréchet, B. De Meester, A. Denquin, T. Pardoen, Sequential modeling of local precipitation, strength and strain hardening in friction stir welds of an aluminum alloy 6005A-T6, Acta Mater. 55 (2007) 6133–6143.
[59] G. Fribourg, Y. Bréchet, A. Deschamps, A. Simar, Microstructure-based modelling of isotropic and kinematic strain hardening in a precipitation-hardened aluminium alloy, Acta Mater. 59 (2011) 3621–3635.
[60] A.D. Rollett, U. Kocks, A Review of the Stages of Work Hardening, Solid State Phenomena, Trans Tech Publ, 1993, pp. 1–18.
[61] U. Kocks, Laws for work-hardening and low-temperature creep, J. Eng. Mater. Technol. 98 (1976) 76–85.
[62] X. He, F. Gu, A. Ball, A review of numerical analysis of friction stir welding, Prog. Mater. Sci. 65 (2014) 1–66.